The Astrophysical Journal, 793:11 (6pp), 2014 September 20 doi:10.1088/0004-637X/793/1/11
© 2014. The American Astronomical Society. All rights reserved. Printed in the U.S.A.

IMAGING THE ENVIRONMENT OF A $z = 6.3$ SUBMILLIMETER GALAXY WITH SCUBA-2

E. I. Robson[1], R. J. Ivison[2,3], Ian Smail[4], W. S. Holland[1,3], J. E. Geach[5], A. G. Gibb[6], D. Riechers[7], P. A. R. Ade[8], D. Bintley[9], J. Bock[10], E. L. Chapin[11], S. C. Chapman[12], D. L. Clements[13], A. Conley[14], A. Cooray[15], J. S. Dunlop[3], D. Farrah[16], M. Fich[17], Hai Fu[15], T. Jenness[7], N. Laporte[18], S. J. Oliver[19], A. Omont[20,21], I. Pérez-Fournon[18,22], Douglas Scott[6], A. M. Swinbank[4], and J. Wardlow[23]

[1] United Kingdom Astronomy Technology Centre, Royal Observatory, Blackford Hill, Edinburgh EH9 3HJ, UK; rob.ivison@gmail.com
[2] European Space Observatory, Karl Schwarzschild Strasse 2, D-85748 Garching, Germany
[3] Institute for Astronomy, University of Edinburgh, Royal Observatory, Blackford Hill, Edinburgh EH9 3HJ, UK
[4] Institute for Computational Cosmology, Durham University, South Road, Durham DH1 3LE, UK
[5] Centre for Astrophysics Research, University of Hertfordshire, Hatfield AL10 9AB, UK
[6] Department of Physics and Astronomy, University of British Columbia, 6224 Agricultural Road, Vancouver, BC V6T 1Z1, Canada
[7] Astronomy Department, Cornell University, Ithaca, NY 14853, USA
[8] Astronomy and Instrumentation Group, Cardiff University, Cardiff, Wales CF10 3XQ, UK
[9] Joint Astronomy Centre, 660 North Ahoku Place, University Park, Hilo, HI 96720, USA
[10] Jet Propulsion Laboratory, National Aeronautics and Space Administration, Pasadena, CA 91109, USA
[11] XMM-Newton Science Operations Centre, European Space Astronomy Centre, Apartado 79, E-28691 Villaneueva de la Canada, Madrid, Spain
[12] Department of Physics and Atmospheric Science, Dalhousie University, Coburg Road, Halifax B3H 1A6, Canada
[13] Astrophysics Group, Imperial College London, Blackett Laboratory, Prince Consort Road, London SW7 2AZ, UK
[14] Center for Astrophysics and Space Astronomy, 389 UCB, University of Colorado, Boulder, CO 80309, USA
[15] Department of Physics and Astronomy, University of California, Irvine, CA 92697, USA
[16] Department of Physics, Virginia Tech, Blacksburg, VA 24061, USA
[17] Department of Physics and Astronomy, University of Waterloo, Waterloo, Ontario N2L 3G1, Canada
[18] Instituto de Astrofsica de Canarias, E-38200 La Laguna, Tenerife, Spain
[19] Astronomy Centre, Department of Physics and Astronomy, University of Sussex, Brighton BN1 9QH, UK
[20] UPMC Univ. Paris 06, UMR 7095, IAP, F-75014 Paris, France
[21] CNRS, UMR 7095, IAP, F-75014 Paris, France
[22] Departamento de Astrofisica, Universidad de La Laguna, E-38205 La Laguna, Tenerife, Spain
[23] Dark Cosmology Centre, Niels Bohr Institute, University of Copenhagen, DK-1165 Copenhagen, Denmark
Received 2014 February 28; accepted 2014 July 19; published 2014 August 28

ABSTRACT

We describe a search for submillimeter emission in the vicinity of one of the most distant, luminous galaxies known, HerMES FLS3, at $z = 6.34$, exploiting it as a signpost to a potentially biased region of the early universe, as might be expected in hierarchical structure formation models. Imaging to the confusion limit with the innovative, wide-field submillimeter bolometer camera, SCUBA-2, we are sensitive to colder and/or less luminous galaxies in the surroundings of HFLS3. We use the Millennium Simulation to illustrate that HFLS3 may be expected to have companions if it is as massive as claimed, but find no significant evidence from the surface density of SCUBA-2 galaxies in its vicinity, or their colors, that HFLS3 marks an overdensity of dusty, star-forming galaxies. We cannot rule out the presence of dusty neighbors with confidence, but deeper 450 μm imaging has the potential to more tightly constrain the redshifts of nearby galaxies, at least one of which likely lies at $z \gtrsim 5$. If associations with HFLS3 can be ruled out, this could be taken as evidence that HFLS3 is less biased than a simple extrapolation of the Millennium Simulation may imply. This could suggest either that it represents a rare short-lived, but highly luminous, phase in the evolution of an otherwise typical galaxy, or that this system has suffered amplification due to a foreground gravitational lens and so is not as intrinsically luminous as claimed.

Key words: galaxies: high-redshift – galaxies: starburst – infrared: galaxies – radio continuum: galaxies – submillimeter: galaxies

Online-only material: color figures

1. INTRODUCTION

Dust extinction and a profusion of less luminous foreground galaxies makes it difficult to select high-redshift ultraluminous star-forming galaxies ($L_{\rm IR} \geqslant 10^{12}\ L_\odot$) at rest-frame ultraviolet/optical wavelengths. Although extinction is not an issue at radio wavelengths, an unfavorable *K*-correction works against detecting the highest redshift examples, $z \gg 3$. Since the advent of large-format submillimeter (submm) cameras such as the Submillimeter Common-User Bolometer Array (SCUBA; Holland et al. 1999), however, it has been possible to exploit the *negative K*-correction in the submm waveband to select dusty, star-forming galaxies (submm-selected galaxies, or SMGs) almost independently of their redshift (e.g., Franceschini et al. 1991; Blain & Longair 1993).

The scope of this field has been substantially expanded by *Herschel* (Pilbratt et al. 2010), which has surveyed approximately 100 deg^2 of extragalactic sky to the confusion limit at 500 μm (as defined by Nguyen et al. 2010), with simultaneous imaging at 250 and 350 μm, using the SPIRE instrument (Griffin et al. 2010). A SPIRE image of the *Spitzer* First Look Survey (FLS) field, obtained as part of the *Herschel* Multi-Tiered Extragalactic Survey (HerMES;[24] Oliver et al. 2012), led to the discovery of 1HERMES S350 J170647.8+584623

[24] hermes.sussex.ac.uk

(hereafter HFLS3; Riechers et al. 2013; Dowell et al. 2014) as an unusually red SPIRE source with $S_{250} < S_{350} < S_{500}$, i.e., with its thermal dust peak within or beyond the 500 μm band (see also Cox et al. 2011; Combes et al. 2012; Rawle et al. 2014). Some of these "500 μm risers" are in fact due to synchrotron emission from bright, flat-spectrum radio quasars (e.g., Jenness et al. 2010), but HFLS3 does not exhibit such powerful active galactic nucleus (AGN)-driven radio emission. Panchromatic spectral-line observations place HFLS3 at $z = 6.34$ via the detection of H_2O, CO, OH, OH^+, NH_3, [C I], and [C II] emission and absorption lines. Its continuum spectral energy distribution (SED) is consistent with a characteristic dust temperature, $T_d = 56$ K, and a dust mass of $1.1 \times 10^9\ M_\odot$. Its infrared (IR) luminosity, $L_{IR} = 2.9 \times 10^{13}\ L_\odot$, suggests a star-formation rate of $2900\ \mu_L^{-1}\ M_\odot\ yr^{-1}$ for a Chabrier (2003) initial mass function, where the lensing magnification suffered by HFLS3 due to a foreground galaxy less than 2″ away has been estimated to be in the range $\mu_L = 1.2$–1.5 (Riechers et al. 2013, although Cooray et al. 2014 estimate $\mu_L = 2.2 \pm 0.3$).

It is expected that the most massive galaxies found at very high redshifts grew in (and thus signpost) the densest peaks in the early universe, making them useful tracers of distant protoclusters. Above $z \sim 6$, such sources may also contribute to the rapid evolution of the neutral fraction of the universe, during the so-called "era of reionization," and to the earliest phase of enrichment of the interstellar medium in galaxies, less than 1 Gyr after the big bang. They may also host the highest redshift quasars. In the submm regime, to explore distant galaxies and their environments, we have observed radio galaxies and quasars, typically detecting a factor ∼2–4× overdensities of submm companions around these signposts (e.g., Ivison et al. 2000; Stevens et al. 2003, 2010; Robson et al. 2004; Priddey et al. 2008). Here, we continue this tradition, targeting the most distant known submm galaxy, HFLS3 at $z = 6.34$, with the 10,000 pixel SCUBA-2 bolometer camera (Holland et al. 2013), which is more sensitive than *Herschel* to cold dust in high-redshift galaxies.

In Section 2, we describe our SCUBA-2 observations of the field surrounding HFLS3, after its discovery with SPIRE on board *Herschel*, and our reduction of those data. In Section 3, we analyze the surface density of SCUBA-2 galaxies in the field, and their color, and discuss whether there is any evidence that HFLS3 inhabits an overdense region of the universe, as might be expected in hierarchical structure-formation models (e.g., Kaufman et al. 1999; Springel et al. 2005). We finish with our conclusions in Section 4. Throughout, we adopt a cosmology with $H_0 = 71$ km s^{-1} Mpc^{-1}, $\Omega_m = 0.27$, and $\Omega_\Lambda = 0.73$, so 1″ equates to 5.7 kpc at $z = 6.34$.

2. OBSERVATIONS AND DATA REDUCTION

2.1. SCUBA-2 Imaging and Catalogs

Data were obtained simultaneously at 450 and 850 μm in 2011 September 23–24 and 2012 March 14 (project M11BGT01) using SCUBA-2 on the 15 m James Clerk Maxwell Telescope (JCMT). The observations were taken with the constant speed DAISY pattern, which provides uniform exposure-time coverage in the central 3′ diameter region of a field, and useful coverage over 12′. A total of 6.9 hr was spent integrating on HFLS3. Observing conditions were good or excellent, with precipitable water vapor levels typically 1 mm or less, corresponding to a 225 GHz optical depth of 0.05. The data were calibrated in flux density against the primary calibrators Uranus and Mars, and also secondary sources CRL 618 and CRL 2688 from the JCMT calibrator list (Dempsey et al. 2013), with estimated calibration uncertainties amounting to 5% at 850 μm and 10% at 450 μm.

The data were reduced using the Dynamic Iterative Map-Maker within the STARLINK SMURF package (Chapin et al. 2013) called from the ORAC-DR automated pipeline (Cavanagh et al. 2008). The chosen recipe accounted for attenuation of the signal as a result of time series filtering and removed residual low-frequency noise from the map using a jack knife method. The maps were made using inverse-variance weighting, with 1″ pixels at both wavelengths, before the application of a matched filter (e.g., Chapin et al. 2011).

The map maker used a "blank-field" configuration file, optimized for faint, unresolved, or compact sources. This applies a high-pass filter with a spatial cutoff of 200″, corresponding to about 0.8 Hz for a typical scanning speed of 155″ s^{-1}. This removes the majority of low-frequency (large spatial scale) noise, while the remainder is removed using a Fourier-space whitening filter. This is derived from the power spectrum of the central 9′ region of a jack knife map, produced from two independent halves of the total data set.

This filtering attenuates the peak signal of sources in the map. To estimate the magnitude of this effect, the pipeline re-makes each map with a fake 10 Jy Gaussian added to the raw data, offset from the nominal map center by 30″ to avoid contamination by any target at the map center. The amplitude of the fake Gaussian in the output map is measured to determine a correction factor. The standard flux conversion factor, as determined from observations of primary and secondary calibrators, is then multiplied by this factor (1.17 and 1.15 at 850 and 450 μm, respectively) and applied to the final image to give a map calibrated in Jy beam^{-1}. The maps with the fake Gaussian are also used to form the point-spread function (PSF) for the matched filter since they reflect the effective point-source transfer function of the map maker.

The SCUBA-2 850 and 450 μm images shown in Figure 1 reach noise levels of 0.9 and 5.0 mJy beam^{-1} over the central 3′ diameter regions, yielding detections of HFLS3 at approximately the 41σ and 7σ levels, respectively. At 850 μm, the central 67.2 arcmin^2 of the map has a noise level of 1.5 mJy beam^{-1} or better. The astrometry of the SCUBA-2 images was found to be accurate to better than 1″ by stacking at the positions of 3.6 μm and 1.4 GHz sources in the field.

Following Geach et al. (2013), we create a catalog of sources from the 450 and 850 μm images by searching for peaks in the beam-convolved signal-to-noise ratio (S/N) maps, recording their coordinates, flux densities, and local noise levels. We then mask a region 1.5 times the beam size and then repeat the search. Above a signal-to-noise level of 3.75, the contamination rate due to false detections is below 5%. We adopt this as our detection threshold, listing the 26 sources with 850 μm flux density uncertainties below 1.5 mJy in Table 1, alongside 450 μm sources selected from the same area at the same significance threshold.

We calculate our completeness levels and flux boosting following Geach et al. (2013), who followed Weiß et al. (2009), injecting 10^5 artificial point sources into a map with the same noise properties as the real image. We correct for false positives using the jack knife map.

2.2. Herschel Imaging

The acquisition and reduction of 16.8 hr of *Herschel* SPIRE and (shallow) PACS data for the FLS field (OD159, 164)

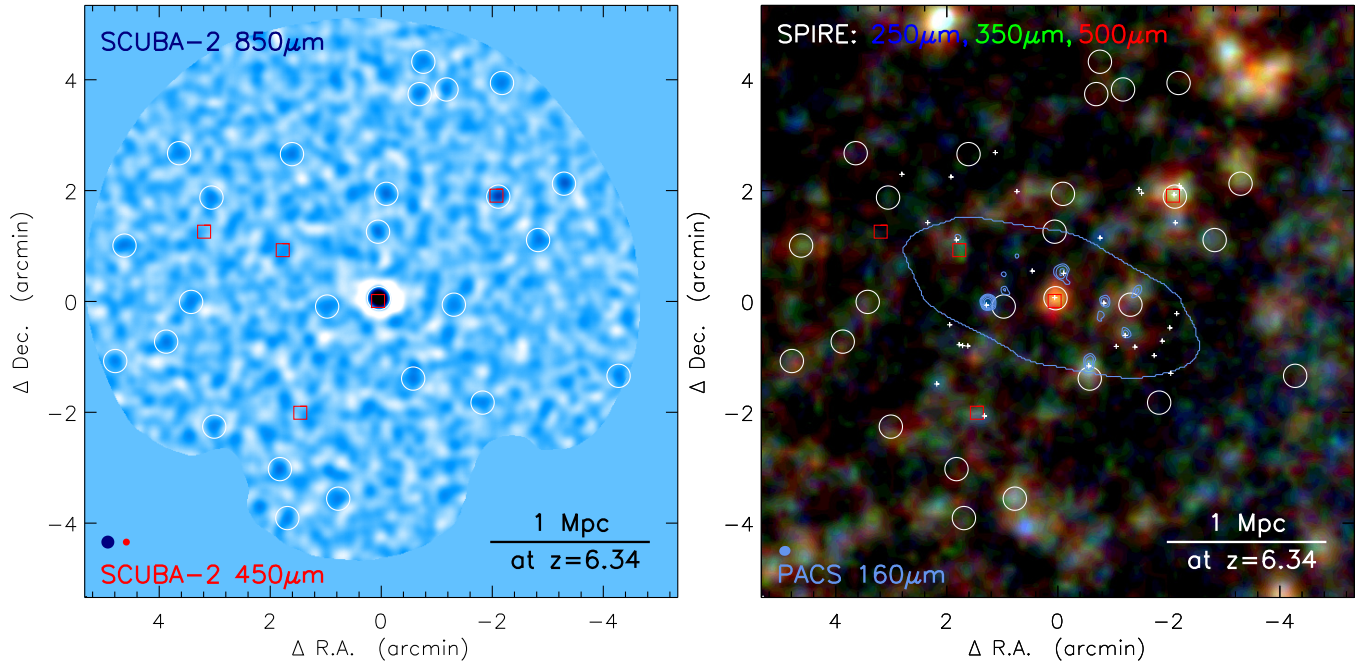

Figure 1. Left: SCUBA-2 imaging at 850 μm, with 450 and 850 μm sources marked by red squares and white circles, respectively, for the 67.2 arcmin^2 where $\sigma_{850} \leqslant 1.5$ mJy beam^{-1}. The negative bowl around HFLS3 is a typical artifact of the filtering procedures employed here. The FWHM of the SCUBA-2 beams are shown as solid ellipses. Right: three-color representation of the data obtained using SPIRE at 250, 350, and 500 μm for the same field around HFLS3, superimposed with blue PACS 160 μm contours. Several of the SCUBA-2 850 μm sources are associated with green SPIRE sources—those with SEDs peaking at 350 μm, consistent with $z \approx 2$; others have no obvious SPIRE counterparts and may lie at considerably higher redshifts. The region over which PACS sensitivity is better than half the best is outlined in blue. Positions of faint 1.4 GHz sources from the $\sim$1.3″ resolution, $\sigma \sim 11$ μJy beam^{-1} Karl G. Jansky Very Large Array imaging described in Riechers et al. (2013) are marked with "+" (the radio catalog covers only $\approx$25% of the region shown, hence the detection rate is unremarkable). North is up and east is to the left; offsets from $\alpha_{2000} = 17{:}06{:}47.8$, $\delta_{2000} = +58{:}46{:}23$ are marked.

(A color version of this figure is available in the online journal.)

as part of HerMES is described in detail by Oliver et al. (2012). The SPIRE data, which are confusion-limited, are shown as a three-color image in Figure 1.

We have obtained much deeper data from PACS (Poglitsch et al. 2010) via a 3.9 hr integration as part of program OT2_DRIECHER_3 (OD1329; see Riechers et al. 2013, for further details). Observations were carried out on 2013 January 1 in mini-scan mapping mode (4 × 15 repeats), using the 70 plus 160 μm parallel mode and the 110 plus 160 μm parallel mode for one orthogonal cross-scan pair each. In the 70, 110, and 160 μm bands, the rms sensitivities at the position of HFLS3 are 0.67, 0.73, and 1.35 mJy beam^{-1}, respectively. Data reduction and mosaicking were carried out using standard procedures. The absolute flux density scale is accurate to 5%. The 160 μm PACS image, the only one potentially useful in the context of faint, distant galaxies, is shown in Figure 1.

The 250, 350, and 500 μm flux densities, S_{250}, S_{350}, and S_{500}, at the positions[25] of the 19 SMGs discussed in Section 2.1 were determined using beam-convolved SPIRE maps. None of our SMGs lie near bright SPIRE sources so we expect the uncertainties associated with these flux densities should be close to the typical confusion levels, $\approx$6 mJy (where, hereafter, we adopt $\sigma_{\rm conf}$ in each SPIRE band from Nguyen et al. 2010).

3. RESULTS, ANALYSIS, AND DISCUSSION

HFLS3 dominates the submm sky in the 67.2 arcmin^2 (8 Mpc^2) region we have mapped at 850 μm with SCUBA-2, being three times brighter than the next brightest submm emitter (Figure 1; Table 1). At 450 μm, HFLS3 is the brightest SMG in the region, despite the peak of its SED having moved beyond that filter; it is one of two sources detected formally at both 450 and 850 μm. Perhaps unsurprisingly, there are no sources in common between the SCUBA-2 and PACS images.

We see no evidence for an overdensity of SMGs on <1.5 Mpc scales around the position of HFLS3 in either our 450 or 850 μm maps (Figure 1).

3.1. Number Counts Relative to Blank Fields

Although no obvious cluster of submm emitters is visible near HFLS3 in Figure 1, we must ask whether the entire 8 Mpc^2 field might be overdense in SMGs. Figure 2 shows the density of sources brighter than S_ν at 450 and 850 μm—extracted at the 3.75σ level and corrected for incompleteness using the analysis discussed in Section 2.1, excluding HFLS3 itself—relative to the source density seen in typical blank-field surveys, where the same techniques have been used to construct catalogs and correct for incompleteness (Coppin et al. 2006; Geach et al. 2013). The only hint of an overdensity comes in the 850 μm bin at 5 mJy, but a $\approx$2σ deviation is not unusual when plotting seven points. Simplifying matters, then, by taking only one large bin above our detection threshold at 850 μm, we find 26 sources (25 if we ignore HFLS3) against an expectation of 20 from Coppin et al. (2006)—on the face of it, a $\approx$1σ overdensity. When we take into account the errors associated with the Coppin et al. (2006) counts, we expect to see 26 (25) sources in a random field of the same size 13% (19%) of the time, so the result obtained intuitively from studying Figure 2 is confirmed—any excess is statistically unconvincing. No significant overdensity of SMGs is apparent in the vicinity of HFLS3, at least not on

[25] Positions are known to $\sigma_{\rm pos} \approx 2''.2$ even for the least significant SMGs, a small fraction of the beam-convolved SPIRE PSF.

Table 1
Sources Detected at 850 and 450 μm Near HFLS3

IAU Name	S (mJy)[a]	S/N
850 μm		
S2FLS850 J170647.67+584623.0[b]	35.4 ± 0.9	40.9
S2FLS850 J170631.07+584812.9	11.4 ± 1.3	8.6
S2FLS850 J170621.93+584826.8	9.3 ± 1.4	6.5
S2FLS850 J170646.64+584816.0	5.6 ± 1.0	5.5
S2FLS850 J170647.80+584735.0	4.9 ± 0.9	5.3
S2FLS850 J170701.41+584318.0	7.5 ± 1.4	5.3
S2FLS850 J170625.54+584725.9	6.3 ± 1.3	4.8
S2FLS850 J170642.92+584456.0	4.7 ± 1.0	4.6
S2FLS850 J170717.24+584535.8	5.8 ± 1.3	4.6
S2FLS850 J170659.77+584859.0	5.6 ± 1.2	4.6
S2FLS850 J170723.05+584719.7	6.1 ± 1.4	4.5
S2FLS850 J170642.00+585004.0	5.4 ± 1.2	4.5
S2FLS850 J170630.54+585015.9	6.2 ± 1.4	4.4
S2FLS850 J170710.97+584811.9	5.4 ± 1.3	4.2
S2FLS850 J170653.32+584246.0	5.5 ± 1.3	4.2
S2FLS850 J170713.78+584618.8	4.9 ± 1.2	4.2
S2FLS850 J170638.27+585009.0	5.3 ± 1.3	4.2
S2FLS850 J170710.54+584403.9	6.1 ± 1.5	4.1
S2FLS850 J170724.30+584514.7	5.9 ± 1.5	4.0
S2FLS850 J170700.38+584225.0	5.9 ± 1.5	4.0
S2FLS850 J170715.48+584859.8	5.4 ± 1.3	4.0
S2FLS850 J170614.39+584458.7	6.0 ± 1.5	4.0
S2FLS850 J170641.49+585039.0	5.3 ± 1.3	4.0
S2FLS850 J170637.26+584616.0	3.9 ± 1.0	3.9
S2FLS850 J170633.28+584430.0	5.2 ± 1.3	3.8
S2FLS850 J170654.87+584614.0	3.3 ± 0.9	3.8
450 μm		
S2FLS450 J170647.80+584620.0[b]	39.8 ± 5.5	7.3
S2FLS450 J170701.05+584715.0	29.4 ± 6.9	4.3
S2FLS450 J170631.33+584813.9	36.3 ± 8.8	4.1
S2FLS450 J170636.12+584224.0	32.5 ± 8.3	3.9
S2FLS450 J170658.59+584419.0	30.2 ± 7.8	3.9
S2FLS450 J170711.99+584734.9	34.5 ± 8.9	3.9

Notes.
[a] Deboosted flux densities; errors exclude 5% and 10% calibration uncertainties at 850 and 450 μm, respectively.
[b] HFLS3.

megaparsec scales at flux densities above the JCMT confusion limit.

3.2. Redshift Constraints for Sources in the Field

The K-correction in the submm waveband means our SCUBA-2 maps are sensitive to SMGs across a very wide redshift range, reducing the contrast of any potential structure around HFLS3. However, with SCUBA-2, SPIRE, and PACS photometry in hand, we are able to crudely constrain the likely redshifts of the galaxies detected in the field surrounding HFLS3, using their far-IR/submm colors. Figure 3 shows color–color plots for HFLS3 and its neighboring SMGs, designed to exploit information from SCUBA-2 at 850 μm to constrain the redshifts of galaxies at $z > 2$ (Ivison et al. 2012), probing their colors across the rest-frame ≈100 μm bump seen in the SEDs of all dusty, star-forming galaxies. The colored backgrounds in the upper and lower panels of Figure 3 indicate the typical redshift of the subset of 10^7 model SEDs that fall in each pixel, where we have adopted a flat redshift distribution (z = 0–7), a flat distribution for the spectral dependence of the dust emissivity (β = 1.8–2.0, centered on the β measured

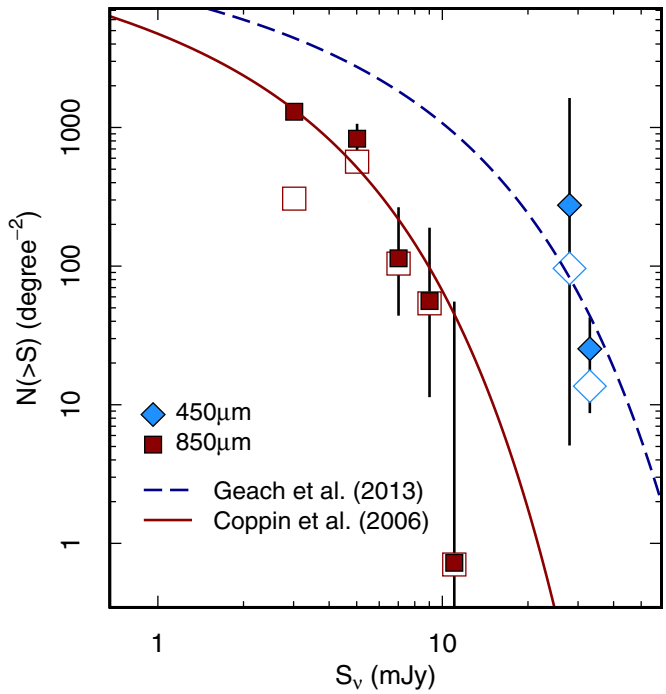

Figure 2. Source counts in several flux density bins at 450 and 850 μm in the 67.2 arcmin^2 region around HFLS3, excluding HFLS3 itself, relative to those found in typical blank fields by Coppin et al. (2006) and Geach et al. (2013). We see no indication of a strong excess of submm emitters across the field, compared to blank-field counts, which suggests there is no overdensity of SMGs on ∼1.5 Mpc scales around HFLS3. The raw counts, uncorrected for incompleteness, are shown as open symbols.

(A color version of this figure is available in the online journal.)

for HFLS3), and 10% flux density uncertainties. For the upper panel of Figure 3, we adopt the dust temperature of HFLS3 (T_d = 56 K).

We concentrate only on those galaxies detected by SCUBA-2, since SPIRE-detected galaxy with a typical SED in the vicinity of HFLS3 could not have evaded detection at 850 μm. Despite its relatively high T_d, HFLS3 is the reddest source detected in the three bands used to make Figure 3.

For SMGs with SPIRE flux densities below $2\sigma_{\rm conf}$, we plot limits based on the measured flux density (zero, if negative) plus $\sigma_{\rm conf}$. We have arbitrarily placed those sources without detections at 350 and 500 μm at $S_{350}/S_{500} = 2$; some could be considerably redder than this in S_{350}/S_{500}, but we cannot constrain this color reliably with the relatively shallow *Herschel* data at our disposal. Several SMGs may also be as red as HFLS3 in S_{850}/S_{500}, perhaps redder. One particularly interesting example is S2FLS850 J170647.80+584735.0, a 5.3σ SCUBA-2 source with no significant SPIRE emission. With $S_{850}/S_{500} >$ 0.9, this SMG likely lies at $z > 5$, with a lower T_d and luminosity than HFLS3.

The lower panel of Figure 3 shows the effect of lowering T_d, illustrating an issue long known to hamper studies of this kind: far-IR/submm colors are sensitive only to $(1 + z)/T_d$ (Blain 1999), i.e., redshift and T_d are degenerate. As a result, our current data does not allow us to conclude with certainty that the environment surrounding HFLS3 contains other luminous, dusty starbursts; however, we can neither rule it out.

Single-dish imaging of this field at 450, 850, 1100, and 2000 μm is possible from the ground, reaching $\sigma_{450} \sim 2.5$ mJy and $\sigma_{2000} \sim 0.1$ mJy over tens of square arcminutes with existing facilities in a few tens of hours. Would these data be capable

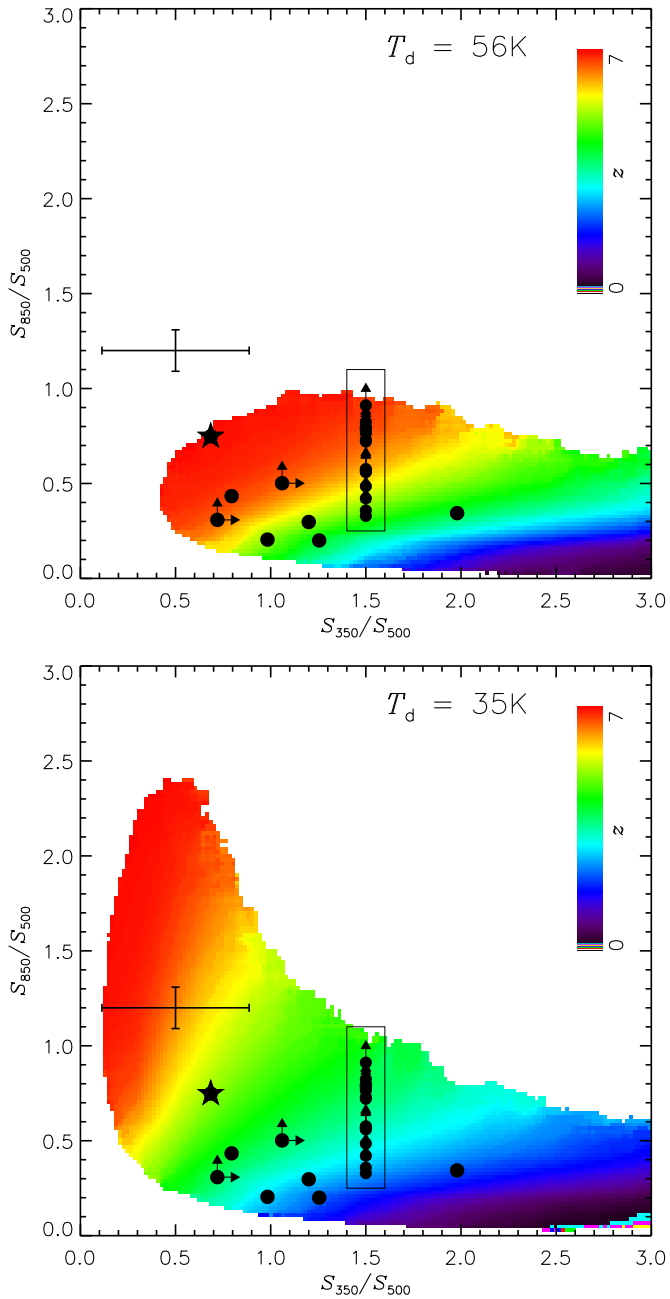

Figure 3. Submm color–color plots for HFLS3 and its neighboring SMGs, adapted from Ivison et al. (2012) and Swinbank et al. (2014). For sources with flux densities below twice the confusion noise ($\sigma_{\rm conf}$; Nguyen et al. 2010), we show limits based on the measured flux density (zero, if negative) plus $\sigma_{\rm conf}$. The colored backgrounds indicate the typical redshift of the subset of 10^7 model SEDs that fall in each pixel, where in the top panel we have adopted the dust temperature of HFLS3 ($T_{\rm d} = 56$ K), a flat redshift distribution from $z = 0$–7, a flat β distribution from 1.5–2.0 (for HFLS3, $\beta = 1.92 \pm 0.12$), and 10% flux density errors. HFLS3 is the star symbol. The error bar is typical for sources detected at 350, 500, and 850 μm. Those sources without detections at 350 and 500 μm are plotted arbitrarily at $S_{350}/S_{500} = 1.5$ inside a rectangular box; some could be considerably redder than this. Of those detected in both 350 and 500 μm, S2FLS J170621.93+584826.8 is the reddest in S_{350}/S_{500}. A handful are as red as HFLS3 in S_{850}/S_{500}, e.g., S2FLS J170647.80+584735.0, which is a 5.3σ SCUBA-2 source with no SPIRE counterpart. Despite its relatively high $T_{\rm d}$, HFLS3 is the reddest of the sources detected in the three bands, though we note that redder objects may exist amongst the SPIRE-undetected SMGs. The lower plot shows a flat β distribution from 1.5–2.0 and $T_{\rm d} = 35$ K, illustrating how $T_{\rm d}$ influences the colors of an SMG. Comparing the redshift constraints from both panels makes it clear that nothing can be usefully concluded about the likely redshifts from the far-infrared colors unless there are independent constraints on the dust temperature.

(A color version of this figure is available in the online journal.)

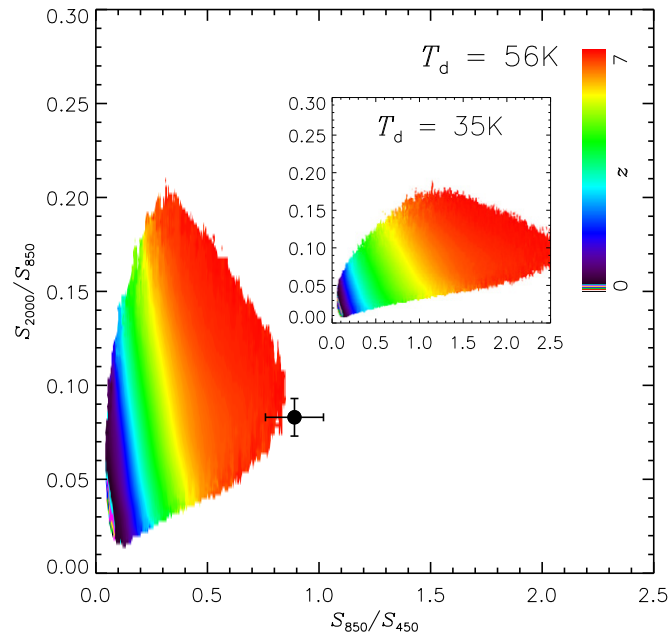

Figure 4. S_{850}/S_{450} vs. S_{2000}/S_{850} ratios for which deep, relatively unconfused and unbiased data can be obtained from the ground, covering tens of square arcminutes. The observed colors of HFLS3 are shown. The colored background indicates the typical redshift of the subset of 10^7 model SEDs that fall in each pixel, where we have adopted the same dust parameters as Figure 3. Inset: same plot, having changed only $T_{\rm d}$, to 35 K, illustrating the degeneracy between redshift and $T_{\rm d}$. $S_{850}/S_{450} \lesssim 0.3$ suggests $z \lesssim 2$ for all but the warmest dust; $S_{850}/S_{450} \gtrsim 1$ suggests $z \gtrsim 5$, with dust much cooler than 35 K unlikely at these redshifts; S_{2000}/S_{850} offers less insight.

(A color version of this figure is available in the online journal.)

of further constraining the redshifts of the SMGs discovered here? Figure 4 shows S_{850}/S_{450} versus S_{2000}/S_{850} and we see that the latter color offers little insight. For $S_{850}/S_{450} \lesssim 0.3$, we can rule out $z \gtrsim 2$ for all but the warmest dust; $S_{850}/S_{450} \gtrsim 1$ suggests $z \gtrsim 5$, even for $T_{\rm d} = 35$ K, with significantly cooler dust unlikely in this redshift regime. Deeper 450 μm imaging would therefore be useful.

3.3. Predictions from the Millennium Simulation

Is the field surrounding HFLS3 less overdense in submm sources than expected for such a massive galaxy living in a biased environment at high redshift, similar to those found around high-redshift radio galaxies and radio-loud quasars at $z = 2$–4 (e.g., Stevens et al. 2003, 2004)? The answer to this question may have implications for the potential gravitational amplification suffered by HFLS3 (see Section 1) or for investigating the potential presence of a buried AGN and its role in supporting its high-IR luminosity.

By necessity this comparison will be crude. We therefore selected the implementation of the Bower et al. (2006) galaxy-formation recipe in the Millennium Simulation (Springel et al. 2005) and searched the $z = 6.2$ output for galaxies with a total baryonic mass in excess of 1.3×10^{11} $M_\odot$, consistent with the combined mass of gas and stars estimated for HFLS3 (Riechers et al. 2013). By adopting a total baryonic mass cut, we are less sensitive to details of the early star-formation histories of galaxies in the model.

We find just one galaxy in the 3.2×10^8 Mpc^3 volume at $z = 6.2$ with a total baryonic mass above 1.3×10^{11} $M_\odot$. All its baryonic mass is in stars; it hosts a 2×10^8 $M_\odot$ black hole and is the central galaxy of a 6×10^{12} $M_\odot$ halo, four times more massive than the next most massive galaxy's halo within the volume, and

the optimal environment to find merging galaxies according to the simulations of Hopkins et al. (2008). Another 16 galaxies are spread across a ~0.7 comoving Mpc diameter region around the most massive galaxy, but most of these are dwarf galaxies with baryonic masses, $\lesssim 10^9\ M_\odot$. Inside a sphere with an angular size of 9′ diameter, centered on the $1.3 \times 10^{11}\ M_\odot$ galaxy, only two galaxies have total baryonic masses of $\gtrsim$15% of the mass of HFLS3 (we choose this limit as the faintest submm emitters in this field have 850 μm flux densities of around 15% that of HFLS3); the next most massive galaxy has half this mass. The total masses of these two companion galaxies in stars and gas are approximately 3 and $4 \times 10^{10}\ M_\odot$ and their predicted $K_{\rm Vega}$ magnitudes are 23.5 and 25.0. The HFLS3 clone is predicted to have $K_{\rm Vega} = 22.5$ for a distance modulus of 49.0, about a magnitude fainter than observed.

From this simple theoretical comparison, we thus expect 2 ± 2 detectable galaxies in the vicinity of HFLS3 if, as expected, their starburst lifetimes are a significant fraction of the time available at this early epoch. This is consistent with the fact that some high-redshift SMGs do have submm-bright companions (e.g., GN 20; Daddi et al. 2009) while others have Lyman-break galaxies nearby but no submm-bright companions (e.g., AzTEC-3; Capak et al. 2011).

Having found no clear evidence for or against the level of overdensity expected in simulations, we can draw no strong conclusions regarding the likely gravitational amplification suffered by HFLS3, or for the likely fraction of its luminosity provided by a buried AGN.

4. CONCLUSIONS

We have detected the most distant, dusty starburst galaxy, HFLS3, at high significance with SCUBA-2. We detect another 29 dusty galaxies within an area of 67.2 arcmin^2 surrounding HFLS3, most of them likely at lower redshift. We find no compelling evidence, from surface density or color, for an overdensity of SMGs around HFLS3, although applying similar selection criteria to theoretical models suggests that a modest excess could be expected, as is found for some other high-redshift SMGs (e.g., GN 20; Daddi et al. 2009). We can therefore draw no strong conclusions regarding the likely gravitational amplification suffered by HFLS3, or for the likely fraction of its luminosity provided by a buried AGN.

We thank John Helly for help with the Millennium Simulation. R.J.I. and I.R.S. acknowledge support from the European Research Council (ERC) in the form of Advanced Investigator programs, COSMICISM and DUSTYGAL, respectively. I.R.S. also acknowledges support from the UK's Science and Technology Facilities Council (STFC, ST/I001573/1), a Leverhulme Fellowship and a Royal Society/Wolfson Merit Award. J.E.G. acknowledges the Royal Society for support. The Dark Cosmology Centre is funded by the Danish National Research Foundation. The JCMT is operated by the Joint Astronomy Centre on behalf of STFC, the National Research Council of Canada and (until 2013 March 31) the Netherlands Organisation for Scientific Research. Additional funds for the construction of SCUBA-2 were provided by the Canada Foundation for Innovation. *Herschel* is an ESA space observatory with science instruments provided by European-led Principal Investigator consortia and with important participation from NASA. SPIRE was developed by a consortium of institutes led by Cardiff University (UK) and including University of Lethbridge (Canada); NAOC (China); CEA, LAM (France); IFSI, Univ. Padua (Italy); IAC (Spain); Stockholm Observatory (Sweden); Imperial College London, RAL, UCL-MSSL, UKATC, University of Sussex (UK); and Caltech, JPL, NHSC, University of Colorado (USA). This development has been supported by national funding agencies: CSA (Canada); NAOC (China); CEA, CNES, CNRS (France); ASI (Italy); MCINN (Spain); SNSB (Sweden); STFC, UKSA (UK); and NASA (USA). The JCMT and *Herschel* data used in this paper can be obtained from the JCMT archive (http://www.jach.hawaii.edu/JCMT/archive) and the *Herschel* Database in Marseille, HeDaM, (http://hedam.oamp.fr/HerMES), respectively.

Facilities: JCMT, *Herschel*

REFERENCES

Blain, A. W. 1999, MNRAS, 309, 955
Blain, A. W., & Longair, M. S. 1993, MNRAS, 264, 509
Bower, R. G., Benson, A. J., Malbon, R., et al. 2006, MNRAS, 370, 645
Capak, P. L., Riechers, D., Scoville, N. Z., et al. 2011, Natur, 470, 233
Cavanagh, B., Jenness, T., Economou, F., & Currie, M. J. 2008, AN, 329, 295
Chabrier, G. 2003, PASP, 115, 763
Chapin, E. L., Berry, D. S., Gibb, A. G., et al. 2013, MNRAS, 430, 2545
Chapin, E. L., Chapman, S. C., Coppin, K. E., et al. 2011, MNRAS, 411, 505
Combes, F., Rex, M., Rawle, T. D., et al. 2012, A&A, 538, L4
Cooray, A., Calanog, J., Wardlow, J. L., et al. 2014, ApJ, 790, 40
Coppin, K., Chapin, E. L., Mortier, A. M. J., et al. 2006, MNRAS, 372, 1621
Cox, P., Krips, M., Neri, R., et al. 2011, ApJ, 740, 63
Daddi, E., Dannerbauer, H., Stern, D., et al. 2009, ApJ, 694, 1517
Dempsey, J. T., Friberg, P., Jenness, T., et al. 2013, MNRAS, 430, 2534
Dowell, C. D., Conley, A., Glenn, J., et al. 2014, ApJ, 780, 75
Franceschini, A., Toffolatti, L., Mazzei, P., Danese, L., & de Zotti, G. 1991, A&AS, 89, 285
Geach, J. E., Chapin, E. L., Coppin, K. E. K., et al. 2013, MNRAS, 432, 53
Griffin, M. J., Abergel, A., Abreu, A., et al. 2010, A&A, 518, L3
Holland, W. S., Bintley, D., Chapin, E. L., et al. 2013, MNRAS, 430, 2513
Holland, W. S., Robson, E. I., Gear, W. K., et al. 1999, MNRAS, 303, 659
Hopkins, P. F., Hernquist, L., Cox, T. J., & Kereš, D. 2008, ApJS, 175, 356
Ivison, R. J., Dunlop, J. S., Smail, I., et al. 2000, ApJ, 542, 27
Ivison, R. J., Smail, I., Amblard, A., et al. 2012, MNRAS, 425, 1320
Jenness, T., Robson, E. I., & Stevens, J. A. 2010, MNRAS, 401, 1240
Kaufman, M. J., Wolfire, M. G., Hollenbach, D. J., & Luhman, M. L. 1999, ApJ, 527, 795
Nguyen, H. T., Schulz, B., Levenson, L., et al. 2010, A&A, 518, L5
Oliver, S. J., Bock, J., Altieri, B., et al. 2012, MNRAS, 424, 1614
Pilbratt, G. L., Riedinger, J. R., Passvogel, T., et al. 2010, A&A, 518, L1
Poglitsch, A., Waelkens, C., Geis, N., et al. 2010, A&A, 518, L2
Priddey, R. S., Ivison, R. J., & Isaak, K. G. 2008, MNRAS, 383, 289
Rawle, T. D., Egami, E., Bussmann, R. S., et al. 2014, ApJ, 783, 59
Riechers, D. A., Bradford, C. M., Clements, D. L., et al. 2013, Natur, 496, 329
Robson, I., Priddey, R. S., Isaak, K. G., & McMahon, R. G. 2004, MNRAS, 351, L29
Springel, V., White, S. D. M., Jenkins, A., et al. 2005, Natur, 435, 629
Stevens, J. A., Ivison, R. J., Dunlop, J. S., et al. 2003, Natur, 425, 264
Stevens, J. A., Jarvis, M. J., Coppin, K. E. K., et al. 2010, MNRAS, 405, 2623
Stevens, J. A., Page, M. J., Ivison, R. J., Smail, I., & Carrera, F. J. 2004, ApJ, 604, L17
Swinbank, A. M., Simpson, J. M., Smail, I., et al. 2014, MNRAS, 438, 1267
Weiß, A., Kovács, A., Coppin, K., et al. 2009, ApJ, 707, 1201